

---

# Light curve cross-correlations of $\gamma$ - and radio data of PKS 0537–441

---

Bachelorarbeit aus der Physik  
vorgelegt von

*Andrea Gokus*

September 29, 2014



Dr. Karl Remeis-Sternwarte Bamberg  
Friedrich-Alexander-Universität Erlangen-Nürnberg

Betreuer:

Prof. Dr. Jörn Wilms  
Prof. Dr. Matthias Kadler



# Contents

<b>1</b>	<b>Scientific Background</b>	<b>9</b>
1.1	Active Galactic Nuclei . . . . .	9
1.1.1	Types of AGN . . . . .	10
1.1.2	General properties of AGN . . . . .	12
1.1.3	One recipe to bake any AGN (Unification Model) . . . . .	13
1.2	The blazar PKS 0537–441 . . . . .	14
<b>2</b>	<b>Very-long-baseline Interferometry (VLBI)</b>	<b>17</b>
2.1	Radio interferometry . . . . .	17
2.2	Imaging with Difmap . . . . .	20
<b>3</b>	<b>Data analysis and results</b>	<b>21</b>
3.1	Gamma-ray observation with <i>Fermi</i> . . . . .	21
3.1.1	The <i>Fermi</i> spacecraft and its instruments . . . . .	21
3.1.2	Creation of the $\gamma$ -ray light curve . . . . .	22
3.2	Radio observation with USNO . . . . .	24
3.2.1	USNO and RRFID . . . . .	24
3.2.2	Imaging and creation of the USNO radio light curve . . . . .	24
3.3	Radio observations with ATCA, Ceduna and TANAMI . . . . .	27
3.3.1	Brief introduction . . . . .	27
3.3.2	Imaging of three TANAMI epochs . . . . .	28
3.3.3	Light curve of all available radio data . . . . .	29
3.4	Cross-correlation between the radio band and $\gamma$ -ray light curves . . . . .	32
<b>4</b>	<b>Discussion and outlook</b>	<b>37</b>
	<b>Bibliography</b>	<b>39</b>



# Zusammenfassung

In meiner Bachelorarbeit führe ich eine Cross-Correlation Analyse für Radio- und Gamma-Emission des Blazars PKS 0537–441 durch. Obwohl es in der Vergangenheit bereits mehrere Multiwellenlängen-Studien zu dieser Quelle gab, sind die astrophysikalischen Mechanismen, die die Emission verursachen, noch immer nicht komplett verstanden.

In meiner Arbeit erstelle ich Lichtkurven mithilfe von Gamma- und Radio-Daten. Die Daten für die Gamma-Emission stammen von *Fermi*/LAT, einem Teleskop, das Gammastrahlung nachweist, und kontinuierlich aktive Galaxien-Kerne (AGN) beobachtet; die Radio-Daten stammen von den Radio-Arrays USNO, TANAMI und ATCA und dem Radio-Teleskop Ceduna, die PKS 0537–441 regelmäßig beobachtet haben. Mithilfe dieser Lichtkurven untersuche ich Zusammenhänge von Radio- und Gamma-Emission.

Da verglichen mit der Gamma-Lichtkurve die Radio-Lichtkurven zerstreut sind, ist eine Cross-Correlation Analyse nur mit den Lichtkurven von Ceduna und *Fermi* möglich. Das Ergebnis der Analyse ist ein zeitlicher Abstand der Lichtkurven von  $\sim 97$  Tagen, wobei die Gamma-Lichtkurve die Leitende von beiden ist. Dies stimmt mit der Annahme überein, dass ein Anstieg der Emission bei AGN im Bereich der Gammastrahlung beginnt und sich dann von hohen Energien zu niedrigen Energien über das gesamte electromagnetische Spektrum hinweg ausbreitet.

Zuvor durchgeführte Studien fanden ebenfalls zeitliche Abstände bei Lichtkurven, diese sind jedoch wesentlich kleiner als die, die in dieser Arbeit präsentiert werden. Daher ist eine Wiederholung der Cross-Correlation Analyse mit kontinuierlicheren Radio-Lichtkurven nötig, um aussagekräftigere Ergebnisse zu bekommen.



# Abstract

In this thesis I present the cross-correlation analysis of the radio- and  $\gamma$ -ray emission of the blazar PKS 0537–441. Many multi-wavelength studies have been performed over the years, but the astrophysical emission mechanisms of this source are still not well understood. With the  $\gamma$ -ray observation by the *Fermi* spacecraft, which observes active galactic nuclei (AGN) continuously, and radio observations from USNO, TANAMI, ATCA and Ceduna on a regular basis, I use the data from these instruments to create light curves. The sparseness of the radio light curves, compared to the  $\gamma$ -ray light curve, complicates the cross-correlation analysis. Eventually, it is only possible to perform cross-correlation with the Ceduna and the *Fermi* light curve. The result of the analysis is a time lag of  $\sim 97$  days, where the  $\gamma$ -ray light curve leads the radio light curve. This is in agreement with the assumption that flares of AGN first appear in the  $\gamma$ -rays, then move energetically downwards across the whole electromagnetic spectrum.

As previous studies found much smaller time lags, it is necessary to repeat the cross-correlation with more continuous radio data samplings in order to get more significant results.



# 1 Scientific Background

The most powerful persistent astrophysical sources are far away from Earth. To reach the nearest of active galactic nuclei (AGN), one has to travel more than 12 million light years through space (Harris et al., 2009). Those objects are of great astrophysical interest as it is desirable to understand the mechanisms working in these sources. The phenomenon of AGN will be introduced in the following by giving an overlook and explaining the physical model of these sources.

## 1.1 Active Galactic Nuclei

The first AGN were unknowingly investigated by Carl Seyfert, who discovered a class of spiral galaxies with a bright and point-like core (Seyfert, 1943). He found strong emission lines being emitted from the central core in the optical spectrum. These were superposed with a common star-like spectrum, which seemed strange since the observed objects were galaxies. With improved radio telescopes and the compilation of the Third Cambridge Catalogue, the discovery of quasars (quasi-stellar radio sources) followed in the 1960s (Bennett, 1962). These point-like sources emit a strong radio signal. Soon after, explanations for this immense radiation were proposed. Lodewijk Woltjer was the first who proposed huge central masses of  $\sim 10^8 M_{\odot}$  for AGN (Woltjer, 1959). As massive objects can accrete matter and thereby release an enormous amount of energy, an accretion process in AGN was introduced by F. Hoyle and W.A. Fowler in 1963. They assumed an accretion disk consisting of gas, which surrounds a massive, stellar-type object. In the same year, Maarten Schmidt (1963) discovered the high redshift of a known AGN. A year later it was proposed by E.E. Salpeter (1964) that the accreting object is a supermassive black hole (SMBH).

Before the first AGN were identified, a strange phenomenon was found in the object M87. H.D. Curtis observed the elliptical galaxy in the Virgo galaxy cluster in 1918 and saw a very long, aligned stream of matter, which was later called jet. In the 1960s, the connection between jets and AGN was recognized: The beginning was marked by the discovery of the coincidence of a radio emission region distant to the core of 3C 274 (M87 in the Messier catalogue) with the brightest spot in the optical jet of M87 (Hogg et al., 1969). With the start of the investigation of 3C sources (radio sources listed in the Third Cambridge Catalogue of Radio Sources), more jets were found in both low- and high-power radio galaxies. The question about the ubiquity of jets however lingered. When the Very Large Array (VLA) went into operation in the 1970s, this uncertainty was clarified because it was able to detect jets with short exposures. It became clear that jets exist in different kinds of the AGN. (Boettcher M. et al., 2012).

### 1.1.1 Types of AGN

Since the 1960s AGN have been investigated at all frequencies and many different subclasses of them have been found, which mostly differ in observational properties. While all AGN emit radio signals, the ratio of the radio flux to the optical flux separates AGN into radio-loud and radio-quiet AGN (see Kellermann et al., 1989):

$$R_{r-o} = \frac{F(6 \text{ GHz})}{F(4400 \text{ \AA})} \quad (1.1)$$

While radio-loud AGN show  $R_{r-o} = 10 - 1000$ , radio-quiet AGN have ratios of  $0.1 < R_{r-o} < 1$ . Radio-loud sources feature jets while radio-quiet sources typically do not show powerful jets. The following discussion is based on Beckmann and Shrader (2012).

#### 1.1.1.1 Radio-quiet AGN

##### Seyfert galaxies

Carl Seyfert described this class of AGN in 1943. This type of galaxies appears to be a normal spiral galaxy, but its core is far brighter and shows strong optical emission with highly ionized emission lines. The Seyfert galaxies can be distinguished into two subclasses: Seyfert I and Seyfert II (Khachikian & Weedman, 1974). Seyfert galaxies are the most common AGN in our local part of the universe, allowing us to study them well. Seyfert I galaxies show broad as well as narrow emission lines, whereas the Seyfert II galaxies seem only to emit narrow lines, which are forbidden. An example of the optical spectrum of both types is shown in Figure 1.1. The broad lines are Doppler-shifted and display velocities

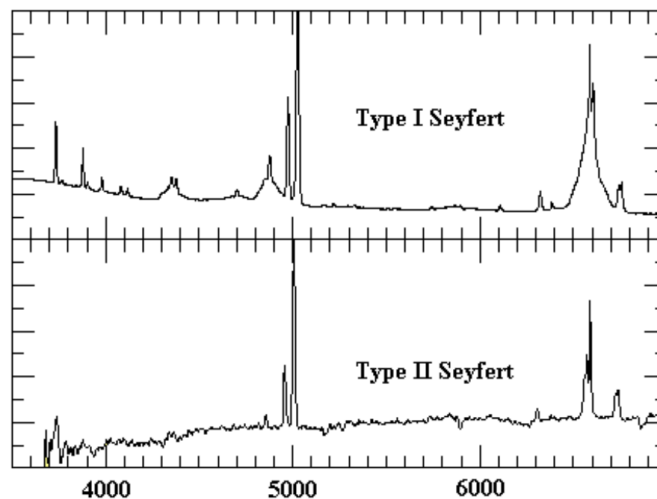


**Figure 1.1:** Optical spectra of a Seyfert I (above) and a Seyfert II galaxy (below). Type I shows broad and narrow lines, Type II only shows narrow lines. (from <http://www.uni.edu/morgans/astro/course/Notes/section3/seyfertspectra.gif> (September 27, 2014))

of  $10^3 - 10^4 \text{ km s}^{-1}$ . Intermediate types, described as Seyfert 1.5 and Seyfert 1.7, exist in addition to Type I and II.

### Radio-quiet quasars

With a bolometric luminosity value of  $M < -21.5 \text{ mag}$ , quasars (quasi-stellar radio sources) are the brightest AGN and show the same optical spectrum as Seyfert galaxies (Vanden Berk et al., 1989). While the host galaxy of a Seyfert AGN is still observable, a quasar outshines its host and makes them appear stellar-like, hence the name QSO (quasi-stellar object). Quasars can also be found in the radio-loud AGN field, but radio-quiet quasars are far more common than their radio-loud counterparts.

#### 1.1.1.2 Radio-loud AGN

AGN with significant radio flux can be divided into radio galaxies and radio-loud quasars, where the latter can be discriminated into some more subclasses, one being blazars. The distinction between the two main types are basically observational differences, e.g. the host galaxy of a radio galaxy is mostly visible in contrary to the host galaxy of a quasar.

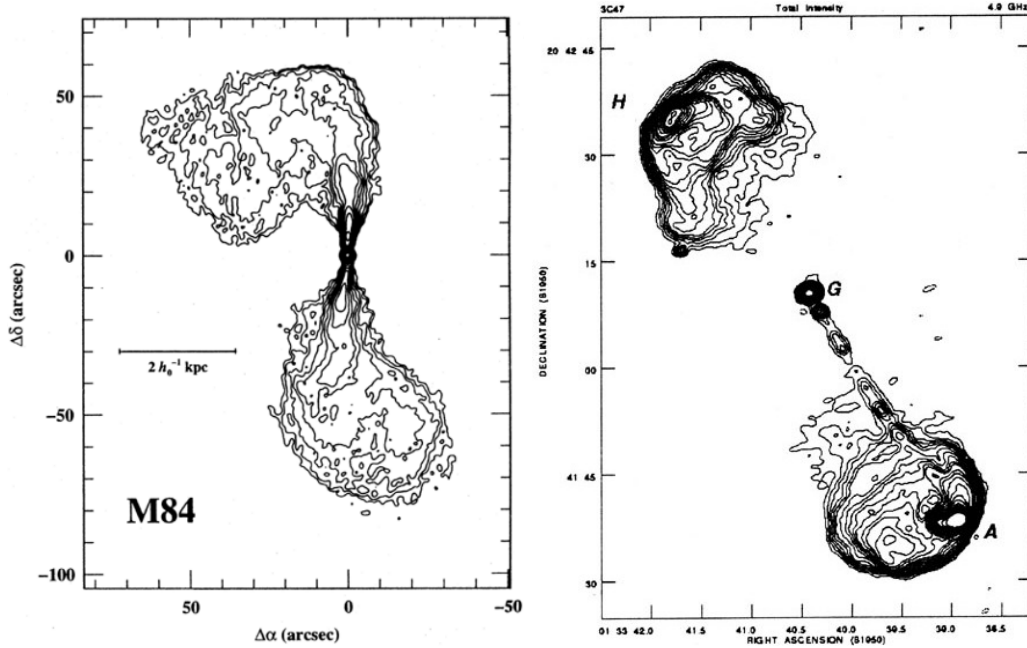
### Radio galaxies

When Fanaroff and Riley analyzed this class of AGN they found that the luminosity of the source correlates with its origin of radiation (Fanaroff & Riley, 1974). The subclass Fanaroff-Riley II AGN (FR II) are far more luminous than subclass Fanaroff-Riley I (FR I). FR I types show a compact emission near the central core, whereas for FR II the radio lobes dominate. Figure 1.2 illustrates the difference. Both types can again be divided into two classes depending on which kind of emission lines is observable. This is a distinction between broad and narrow lines, similar to the case of Seyfert galaxies. If broad and narrow emission lines are observable, it is called a broad-line radio galaxy (BLRG), otherwise, without broad and only narrow lines, it is named a narrow-line radio galaxy (NLRG).

### Radio-loud quasars

Quasars can be separated into many different subclasses. The important subclass for this thesis are blazar, which is why only those are introduced here.

Blazars have a compact radio structure, because their jet is observed at a very small inclination angle to the earth. This gave blazars their name, because they seem to blaze the outflowing material from the core in the direction of the Earth. Those sources are very variable throughout the whole electromagnetic spectrum. Blazars can either be BL Lac objects or Flat Spectrum Radio Quasars (FSRQs). When the first BL Lac type was discovered, it was primarily interpreted as a highly variable star in the constellation Lacerta (Hoffmeister, 1929). They have no significant optical spectrum and very narrow emission lines. BL Lacs vary from FSRQ in the equivalent width of their emission lines, the assumptive limit for this is  $5 \text{ \AA}$ . FSRQs can be distinguished into Highly Polarized Quasars (HPQ), which additionally display polarization, and Optical Violent Variables (OVVs).



(a) Fanaroff-Riley I M84 (Laing R. & Bridle A., 1987, figure by R. W. Pogge) (b) Fanaroff-Riley II 3C 47 (Bridle A.H. et al., 1994)

**Figure 1.2:** Comparison of both Fanaroff-Riley Type I (left picture) and Type II (right picture). FR I shows strong radio emission near the core, whereas FR II has prominent radio lobes.

### 1.1.2 General properties of AGN

Despite the large "zoo" of different AGN, it is generally agreed that the different types of AGN are in fact physically connatural (AGN unification). They are subject to the same overall phenomenon as all of them generate their energy through accretion, which is the most effective energy mechanism. Depending on the mass of its supermassive BH in the center, each AGN has a defining maximum luminosity, which results from the equation of gravitation and radiation pressure. The maximum luminosity is given by the Eddington luminosity

$$L_{\text{Edd}} = \frac{4\pi GMm_p c}{\sigma_T} \simeq 1.3 \cdot 10^{38} \frac{M}{M_\odot} \text{ erg s}^{-1} \quad (1.2)$$

where  $M$  is the mass of the central black hole,  $M_\odot$  the mass of the sun,  $m_p$  the mass of a proton,  $c$  is the speed of light,  $G$  the gravitational constant and  $\sigma_T$  is the Thomson scattering cross-section. If one assumes a SMBH has a mass of  $M = 10^6 M_\odot$ , the maximum luminosity results in  $L_{\text{Edd}} = 1.3 \cdot 10^{44} \text{ erg s}^{-1}$ . Converted into solar luminosity the total maximum flux of the AGN reaches  $L_{\text{Edd}} = 10^{11} L_\odot$ . As a galaxy has about  $10^{11}$  stars on average, the compact center of an active galaxy is as bright as the galaxy itself.

Figure 1.3 depicts this very well: While the galaxy NGC 3783 cannot be seen in the left picture, where the luminosity intensity scale is set to linear, only the AGN is visible. Only after changing the scale to logarithmic does the whole galaxy appear in the picture.

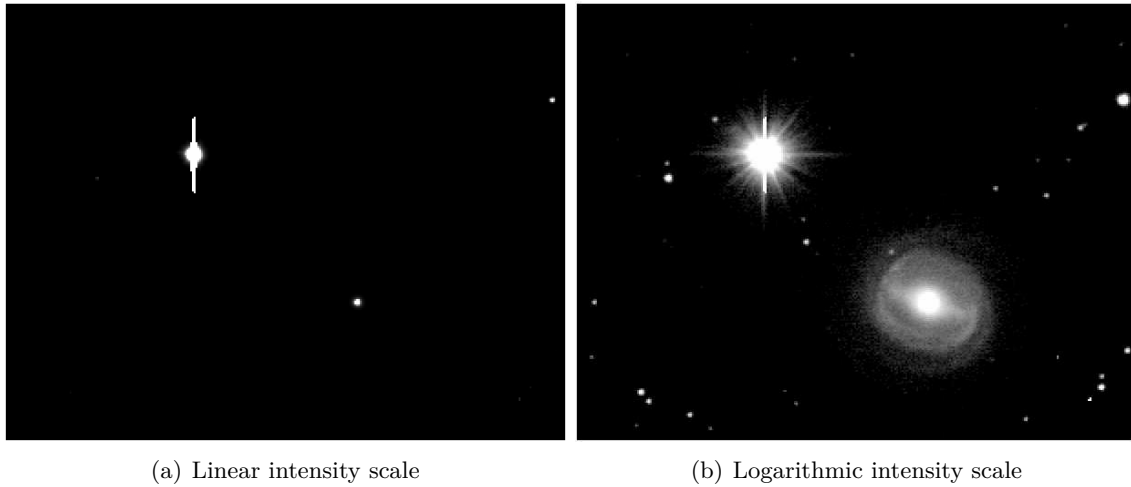


**Figure 1.3:** Comparison of a linear and a logarithmic intensity scale in the optical at NGC 3783: the galaxy bottom right of the right picture is only visible when the luminosity is scaled logarithmic, while the nucleus is clearly visible on the left. The source top left in the pictures is a star. (J. Wilms, priv. comm.)

### 1.1.3 One recipe to bake any AGN (Unification Model)

A demonstrative summary of the unification of AGN was introduced by Urry and Padovani in 1995. The model to describe the varying appearances of AGN is shown in Figure 1.4. The shown model there is for radio-loud AGN, but it is similar for radio-quiet AGN apart from the jet.

The central engine of each AGN is a SMBH ( $M \approx 10^8 M_{\odot}$ ), surrounded by an accretion disk ( $r \sim 10^{-3}$  pc). Above, highly ionized clouds move with velocities from  $10^3$  to  $10^4$  km/s, creating broad emission lines. This region is thereby called broad line region (BLR). Surrounding the central engine, a dusty torus ( $r \sim 1$  pc) blocks optical light when viewed edge on. Then the BLR is not visible anymore. The most extended region however is the narrow-line region (NLR) with  $r \sim 10 - 1000$  pc, which can still be observed with the torus in the line of sight.

Therefore the different appearances result from different angles onto the observed AGN, but they still differ in the power of their emission and whether they have a jet. In Figure 1.5 the different viewing angles onto an AGN are illustrated. If the torus obscures the BLR from the viewer, only narrow emission lines can be observed, which leads to a classification as an Seyfert II (if no jet is present), FR I NLRG

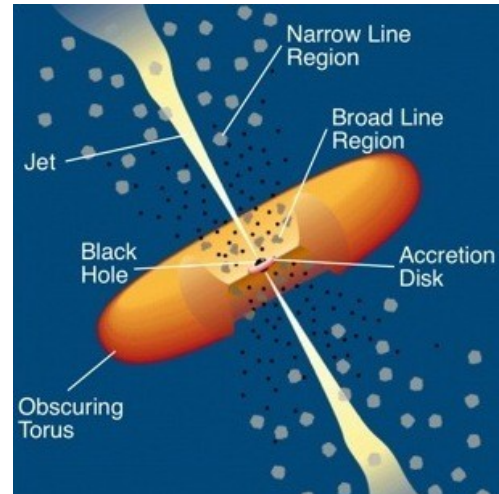


**Figure 1.4:** Illustration of the unified AGN model (Urry & Padovani, 1995).

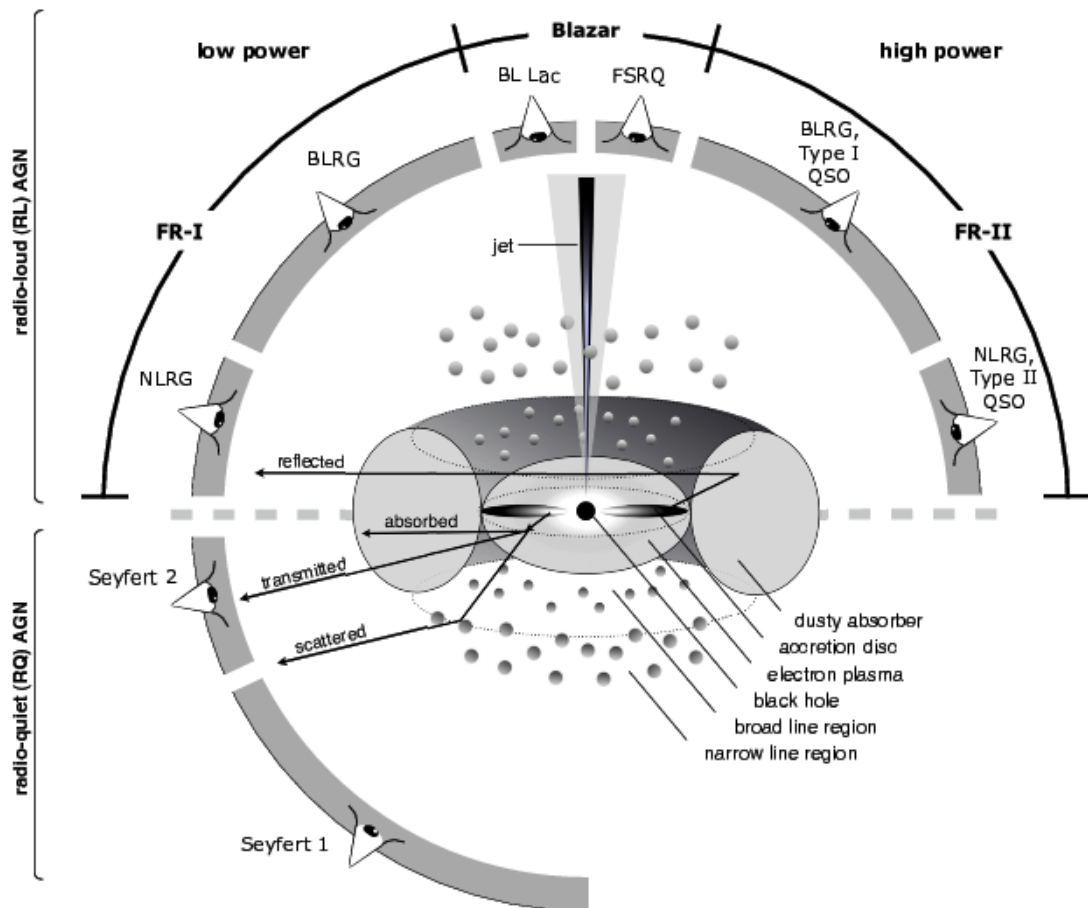


**Figure 1.5:** Illustration of the different types of AGN. Depending on the viewing angle, one can see right to the central engine or the torus blocks the view. The main distinction is the presence of a jet, which defines radio-loud AGN, and the power of the central engine. Note: Radio-loud AGN always emit a jet symmetrically in opposite directions. (Beckmann & Shrader, 2012, p. 132)

(for low power AGN) or FR II NLRG (for high power AGN).

Whenever the BLR is visible, the classification scheme is similar. If the jet is pointing directly at the observer, the AGN is classified as a blazar.

## 1.2 The blazar PKS 0537–441

Found as a quasi-stellar source in the Parkes 2700 MHz radio survey (Peterson et al., 1976) and classified as a blazar (Burbidge & Hewitt, 1992), the AGN PKS 0537–441 might also be a transitional object between classical BL Lac objects and highly polarized and violently variable quasars (Treves et al., 1993; Giommi et al., 1995; Ghisellini et al., 2011). The

source has a redshift of  $z = 0.894$  (Peterson et al., 1976). The optical counterpart of PKS 0537–441 has been observed with the Harvard Observatory photographic plate collection over almost a century, so that William Liller found long-term variability of  $\sim 5$  mag with fluctuations of  $\sim 2$  mag over two months or less (Liller, 1974). Additionally, the source revealed intraday variabilities at optical (Heidt & Wagner, 1996; Romero et al., 2002) and radio frequencies (Romero et al., 1995).

Early multifrequency observations in the 1980s showed quasi-simultaneous flares at infrared, optical and X-ray frequencies (Maraschi et al., 1985; Tanzi et al., 1986). The latest study of correlations across the electromagnetic spectrum was presented by D’Ammando et al. (2013). They used long-term monitoring by *Fermi* and multiwavelength observations by *Swift*<sup>1</sup> (optical to X-ray), SMA<sup>1</sup> (sub-mm), ATOM<sup>2</sup>, and REM<sup>3</sup> (both near-infrared to optical bands).

Next to the analysis of the behaviour of the source from X-ray to mm and the modelling of SEDs, a search for correlations between the different bands was performed with the Discrete Cross-Correlation Function by Edelson & Krolik (1988). The main goal of this procedure is to find similar behaviour in long-term variability and short-term variations at different frequencies. Using non-detrended light curves, D’Ammando et al. found a time lag of  $3.1 \pm 1.9$  days between the  $\gamma$ -ray light curve and the combined R-band data of ATOM and REM at a correlation coefficient of  $0.92 \pm 0.06$ . Another correlation between  $\gamma$ -ray and K-band emission shows a weaker correlation coefficient of  $0.54 \pm 0.07$  at a time lag of  $1.9 \pm 2.5$  days. For detrended light curves the correlation coefficient is significantly smaller with time lags near zero. The positive time lags denote that the  $\gamma$ -ray emission leads radio emission, although the time lag is near zero. No correlation has been found between X-ray and near-infrared or optical bands. In conclusion the paper gives several new results, but proposes more long-term observations to explain the astrophysical mechanism happening at PKS 0537–441.

The reason why this specific AGN was chosen for the analysis presented in this thesis is its brightness in the  $\gamma$ -rays, which is high compared to the luminosity of other blazars in this emission range. Therefore it is a well observed source, which allows us to study the properties of blazars.

PKS 0537–441 has been the target of several multi-wavelength observations since the 1980s, but only with the *Fermi* telescope launched in 2008 (see Section 3.1.1), it was possible to continuously monitor the source during flaring states as well as low activity states. Using this advantage and the continuous observations of multiple radio telescopes and arrays, the search for correlations between radio- and  $\gamma$ -ray emission is possible. Results might give insights into astrophysical processes of blazars.

---

<sup>1</sup>Sub-Millimetre Array: <http://www.cfa.harvard.edu/sma/> (September 27, 2014)

<sup>2</sup>Automatic Telescope for Optical Monitoring for H.E.S.S.: <http://www.lsw.uni-heidelberg.de/projects/hess/ATOM/> (September 27, 2014)

<sup>3</sup>Rapid Eye Mount telescope: <http://www.eso.org/public/teles-instr/lasilla/rem/> (September 27, 2014)



## 2 Very-long-baseline Interferometry (VLBI)

As the mechanism of jet formation is not understood yet, one has to look into the innermost regions of AGN. To resolve these small scale structures of jets, one needs high resolutions below arcseconds, because of the great distance of AGN to the Earth. For example the nearest AGN, Centaurus A, is at a distance of  $\sim 3.8$  Mpc, which means that with an angular resolution of one arcsecond one could resolve a region of 18 pc. Remembering the dimensions of structures in AGN (described in Section 1.1.3), it is clear, that one can not resolve the core and the region where jets are formed at all. Increasing the resolution to milliarcseconds (mas) will improve the resolution by a factor of  $10^3$ , which leads to the possibility of resolving structures with dimensions of  $\sim 0.018$  pc (Müller, 2010). The resolution of a telescope can be enhanced by increasing its diameter. Instead of building a radio telescope with a large dish, which is limited very soon due to constructional boundaries, one can observe the source with many radio telescopes at the same time, creating an interferometer. The telescopes do not have to be connected, but it is crucial to gather exact data about the time and position of the operating telescopes. The basic principles of interferometry are explained in the following. The information is based on the book by Burke and Graham-Smith (2010).

### 2.1 Radio interferometry

The angular resolution of a telescope is defined by the Rayleigh criterion

$$\sin(\alpha) \approx 1.22 \frac{\lambda}{D} \quad (2.1)$$

where  $\alpha$  is the angular resolution,  $\lambda$  is the wavelength and  $D$  is the diameter of the dish. If the wavelength of the observation is fixed, the resolution can only increase by increasing the diameter  $D$ . The first thing to think about is building larger radio telescopes, but the limitations to this are reached quite fast, e.g. the largest radio telescope in Europe is the Effelsberg radio telescope<sup>1</sup> in Germany with a dish of 100m. The solution to this problem is radio interferometry, in which two telescopes observe a source at the same time. They are separated by a distance of  $b_\lambda$  (normalized to the wavelength of the signal), which replaces the diameter  $D$  in the equation. Figure 2.1 shows the two-element Michelson interferometer, which works like one big radio telescope with diameter  $b$ .

---

<sup>1</sup><http://www.mpifr-bonn.mpg.de/effelsberg> (September 27, 2014)

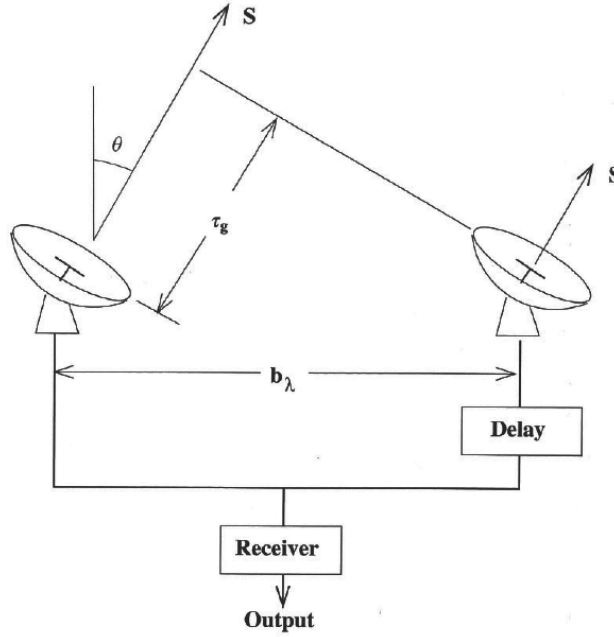


**Figure 2.1:** Geometry of a two-element Michelson interferometer.  $\tau_g$  is the geometrical path delay, which is compensated by the delay circuit in the receiver. Additionally, a delay  $\tau_i$  can be inserted by this delay circuit. (Burke & Graham-Smith, 2010, p. 76)

The time delay  $\tau_g$  has to be taken into account because of the different arrival of the radio signal. It can be calculated as:

$$\tau_g = \frac{b}{c} \sin(\theta) \quad (2.2)$$

Here  $b$  is the length of the baseline and  $c$  is the speed of light.

After the observation, the data is correlated by integrating and multiplying the voltage signals from both telescopes over a time constant. The result is the cross power product

$$R_{xy}(\tau_g) = A(\vec{s})S \cos(2\pi\nu\tau_g) = A(\vec{s})S \cos\left(\frac{2\pi\nu b \sin(\theta)}{c}\right) \quad (2.3)$$

where  $A(\vec{s})$  is the effective area,  $S$  is the source flux and  $\vec{s}$  is the direction of the telescopes. The instrumental time delay  $\tau_i$  is now used to define the reference position  $\vec{s}_0$  (called the *phase-tracking centre*), at which  $\tau_i = \tau_g$ . There  $\tau_i$  settles the geometrical delay  $\tau_g$ . The position of the source can now be specified by using the phase-tracking centre:

$$\vec{s} = \vec{s}_0 + \vec{\sigma} \quad (2.4)$$

$\vec{\sigma}$  is a small vector, which is normal to  $\vec{s}_0$ . The recorded signal of the observation is a convolution of the observed sky and the synthesized beam of the array. The *Visibility function*  $V$  is the measure of an interferometer, giving the Fourier transform of the brightness distribution in the sky

$$V = \int A(\sigma)B_\nu(\sigma) \exp(i2\pi\vec{b}\vec{\sigma})d\Omega \quad (2.5)$$

where  $\vec{b}$  is the baseline vector between two telescopes and  $B_\nu(\sigma)$  is the brightness of the source.

The natural coordinate system for the resulting correlation of the interferometer is a right-handed rectilinear system  $(u, v, w)$ , where  $\vec{s}_0$  corresponds to the  $w$ -direction. The plane perpendicular to the source direction is the  $u, v$ -plane, see Figure 2.2. The unit of the coordinate system is given in wavelengths. The visibility function then becomes

$$V(\vec{s}_0, u, v) = \int A(l, m) B_\nu(l, m) \exp[i2\pi(ul + vm + wn)] d\Omega \quad (2.6)$$

where  $l, m, n$  are the direction cosines of the unit vector  $\vec{s}$  and the coordinates of  $\sigma$  are  $(l, m)$ . Because  $\vec{s}_0$  is perpendicular to the  $u, v$ -plane,  $w = 0$ . The solid angle for the integration over the source is given as

$$d\Omega = \frac{dldm}{\sqrt{1-l^2-m^2}} \quad (2.7)$$

This gives a visibility function that shows clearly that  $V(u, v)$  is a Fourier transform of a modified source brightness

$$V = \int A(l, m) B_\nu(l, m) \exp[i2\pi(ul + vm)] \frac{dldm}{\sqrt{1-l^2-m^2}} \quad (2.8)$$

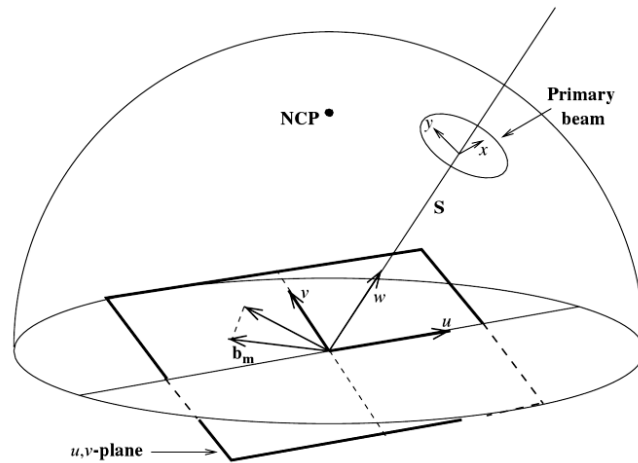


**Figure 2.2:** The geometrical relationship of interferometer, celestial source and  $(u, v)$ -plane; NCP stands for North Celestial Pole. (Burke & Graham-Smith, 2010, p. 83)

In order to reconstruct the brightness distribution, which is basically the source image, the  $(u, v)$ -plane should be well sampled. This can be achieved by both including more telescopes to the VLBI and using the Earth's rotation to change the baseline vector, which makes it time-dependent. Together the changing vector and the additional baselines from additional telescopes create a denser coverage of the plane. With more data sampling it is possible to achieve a better reconstruction of the image.

## 2.2 Imaging with Difmap

Data sets from VLBI can be imaged with `Difmap`<sup>2</sup>. The following description of the program is based on the `Difmap Cookbook` by Greg Taylor (1997), the Diploma thesis of Cornelia Müller (2010) and the Bachelor thesis of Alexander Kappes (2013).

Before the data can be imaged, it has to be calibrated, which will not be discussed in this thesis. For this process see Mueller (2010). As the image of the source is a Fourier transformation, a deconvolution is required. This process can only be performed numerically with the `clean`-algorithm, which creates a model for the visibility function  $V(u, v)$  that gives the solution to the Fourier transformation. Before performing the algorithm, the data is first weighed to shape the dirty beam, which is the Fourier transformed  $(u, v)$ -plane. The TANAMI data in this thesis were weighed by *natural weighting*, which is one of the most common schemes and weights every visibility alike:

$$W_{j,k} = 1 \tag{2.9}$$

with  $j, k$  is the  $j, k$ -th cell. The main advantage for this is the higher sensitivity by having a maximum signal-to-noise ratio. The *uniform weighting* is the second of the most common weighting schemes and leads to a higher resolution. The visibilities then are weighted as follows:

$$W_{j,k} = \frac{1}{\text{number of visibilities in } j, k} \tag{2.10}$$

After fixing the weighting, the  $(u, v)$ -data are being averaged over time (here 32 minutes). A first look at the data regarding their phase, amplitude and error bars is useful to identify data that have unusually large errors or are erroneous due to measurement problems. These data can be flagged, which means they will not be taken into account for the `clean`-algorithm. The assumption for the `clean`-algorithm is that the image of the source is generally composed of point sources. Those are modelled into the dirty map, which is the convolution of the dirty beam and the brightness distribution. The components of the model are set in rectangular "`clean windows`" with which one manually marks the region of the brightest residual. Only in these windows the algorithm is applied. The model components are subtracted from the dirty map at the position of maximum brightness for every new `clean`-iteration.

After each iteration a phase self-calibration should follow additionally, in order to correct changes, which occur due to the subtraction of the components. The `clean`-iteration is applied a few times, creating several model components. This process is repeated until there are no more features in the dirty map, which is now called the "residual map" and only contains the noise of the observation. The generated `clean`-model is convolved with the "clean beam", which is a Gaussian approximation of the full width half maximum of the dirty beam. The "clean map" and the "residual map" together form the final map, which shows the true radio emission of the observed source.

Additionally to this algorithm some self-calibrations are applied. An important one is the amplitude self-calibration, which corrects the overall telescope amplitude. This should be performed in combination with a phase self-calibration after an acceptable model is created. It is important to carefully perform the imaging, because a bad model can lead to a wrong residual map by losing data, which then falsifies the final map.

<sup>2</sup><ftp://ftp.astro.caltech.edu/pub/difmap/difmap.html> (September 4, 2014)

## 3 Data analysis and results

### 3.1 Gamma-ray observation with *Fermi*

#### 3.1.1 The *Fermi* spacecraft and its instruments

The *Fermi Gamma-ray Space Telescope*<sup>1</sup> was launched on June 11<sup>th</sup> 2008 and has been observing the  $\gamma$ -ray sky at an energy range from 10 keV to 300 GeV since. *Fermi* was built in order to observe and study sources that emit  $\gamma$ -ray radiation, e.g., AGN and  $\gamma$ -ray bursts (GRBs). There are two instruments on *Fermi*. The Large Area Telescope (LAT) is the main instrument. Its primary purpose is to give a monitoring of the sky at all times, therefore it scans the whole sky every three hours. The telescope is able to observe 20% of the sky at each moment and covers the energy range from  $\sim 20$  MeV to 300 GeV.

As  $\gamma$ -rays can neither be refracted nor reflected, this kind of emission has to be detected otherwise. When a high energy photon strikes matter, the photon converts into an  $e^+e^-$  pair. Those particles trigger a particle shower which can be measured by the instruments on the telescope. In respect to the operating mode of the telescope it is called a pair-conversion telescope. It consists of four subsystems, which will be introduced briefly. For more detailed information see Atwood et al. (2009). The first subsystem is a so called precision converter-tracker. It consists of 16 planes of high-Z material that triggers the conversion process of  $\gamma$ -rays into  $e^+e^-$  pairs. The passage of the charged particles is recorded with position-sensitive detectors which interlace the converter planes. By measuring the way of  $e^+$  and  $e^-$  the tracker is able to



**Figure 3.1:** Artistic impression of the *Fermi* satellite orbiting the earth.

Credit: NASA

<sup>1</sup>[http://www.nasa.gov/mission\\_pages/GLAST/spacecraft/](http://www.nasa.gov/mission_pages/GLAST/spacecraft/) (September 2, 2014)

reconstruct the direction of the original  $\gamma$ -rays. Additionally the converter-tracker is able to reject background noise by measuring and recording the time-over-threshold (TOT). Therefore this system highly reliably works as the principal trigger for the LAT instrument. The second subsystem is the calorimeter, which measures the energy deposition resulting from the particle shower and images the shower development profile. It consists of 96 CsI(Tl)crystals. The calorimeter works as a background discriminator and an estimator of the shower energy leakage fluctuations.

The anticoincidence detector (ACD) is the third subsystem and provides charged-particle background rejection for charged particles that singly enter the field of view of the LAT. During the electromagnetic shower secondary particles (mostly photons with much lower energies than the original  $\gamma$ -rays) can Compton scatter in the ACD and create false data. The probability of this incident is drastically reduced by segmenting the ACD.

The fourth subsystem is the data acquisition system (DAQ), where the data from the other subsystems is collected and the multilevel event trigger is implemented. It also runs filter algorithms and procures a science platform for the search for transients.

Working as a complement to the LAT, the GLAST Burst Monitor (GMB) is the second instrument on *Fermi*. It is able to observe a wide part of the entire sky and can detect GRBs. The observed energy range overlaps with the one of the LAT, which makes a combination of both instruments quite effective.

### 3.1.2 Creation of the $\gamma$ -ray light curve

The analysis of *Fermi* data is performed by using the *Fermi* Science Tools<sup>2</sup> (provided by the *Fermi* Science Support Center and the LAT instrument team). Working with the Tools, I used scripts written by Bill McConville, Alicia Schooley and Cornelia Müller. In this chapter I will briefly overview the fundamental steps of the analysis, a detailed demonstration can be found at [http://fermi.gsfc.nasa.gov/ssc/data/analysis/scitools/likelihood\\_tutorial.html](http://fermi.gsfc.nasa.gov/ssc/data/analysis/scitools/likelihood_tutorial.html).

For this analysis the data from the 4<sup>th</sup> of August 2008 (*Fermi* start of observations) to 10<sup>th</sup> of May 2014 were taken into account. The performed analysis is an unbinned likelihood analysis, where each bin combines 14 days of measured flux. The exact coordinates of the source PKS 0537–441 are  $\alpha = +84.70984$  Right ascension and  $\delta = -44.08582$  declination, a radius of interest of  $7^\circ$  was used. The energy range spans from 100 MeV to 300 GeV.

First, only the required photons must be filtered, which is done by *gtselect*. A problem occurs if the spacecraft is below a rocking angle  $> 52^\circ$ . Those erroneous photons can be excluded by running *gtmktime*. This function accesses the spacecraft data file, which consists of all information about the *Fermi* spacecraft since its launch. The next tool *make2FGLxml.py* is a script by T. Johnson. Here the spectral index is fixed. It reads a model from an XML file that reverts to two years of observation. The file contains all important sources from the 2FGL catalogue, which are in my radius of interest around PKS 0537–441, and their position as well as the spectral model of each. With the read model an input spectrum is created. Based on the spectrum, which is generated for every bin, the flux can be determined by running the tool *gtlike*, which calculates the maximum likelihood method. Finally the

<sup>2</sup><http://fermi.gsfc.nasa.gov/ssc/data/analysis/> (September 17, 2014)

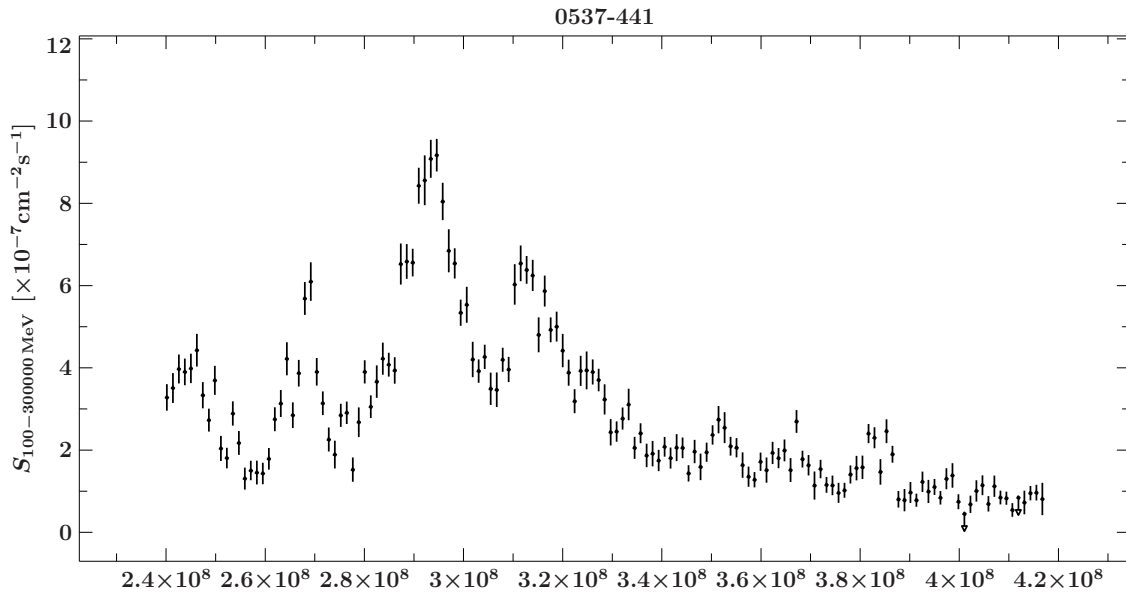


**Figure 3.2:**  $\gamma$ -ray light curve using *Fermi* data. The time is given in MET (mission elapsed time) in seconds. The reference time is January 1, 2001, UTC.

light curve is created.

The resulting light curve is shown in Figure 3.2. Two major flares are visible, where the brightest one happened at the beginning of 2010 and the second occurred almost a year later. Before the first major flare two flares can be seen in the first half of 2009 and the second half of 2008. After the second major flare the source seems to decrease in brightness in  $\gamma$ -rays.

## 3.2 Radio observation with USNO

### 3.2.1 USNO and RRFID

The U.S. Naval Observatory (USNO)<sup>3</sup> collects a wide span of astronomical data. Amongst other things, it regularly takes images of AGN with the National Radio Astronomy Observatory (NRAO) Very Long Baseline Array (VLBA) telescope<sup>4</sup>. The array consists of ten radio telescope antennas, each with a dish of 25 meter diameter. The antennas were built in the VLBA construction to work together for VLBI as ideal as possible. The purpose for USNO is to monitor many active galaxies and observe variability as well as changes in structure. The images are taken in the S- (2.3 GHz), X- (8.4 GHz), K- (24 GHz) and Q-band (43 GHz). In this thesis only data from the S/X-band are analyzed. All data are collected in the Radio Reference Frame Image Database (RRFID).

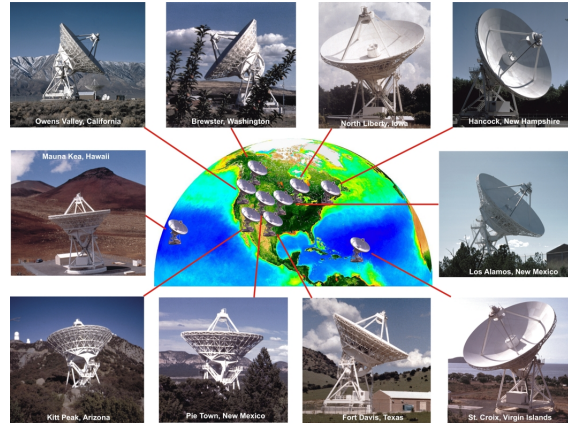


**Figure 3.3:** VLBA telescopes and their position in North America.

Credit: Image courtesy of NRAO/AUI and Earth image courtesy of the SeaWiFS Project NASA/GSFC and ORBIMAGE

### 3.2.2 Imaging and creation of the USNO radio light curve

AGN provide corrections for coordinates on Earth on GPS if it is assumed that they are point sources. This might be an incorrect assumption and has to be checked for each source, imaged and modelled with a jet. The data set consisted of 29 data points in the S-band and the X-band respectively. Starting in July 1995, the monitoring of the source continued until June 2010.

The data of PKS 0537–441 were already calibrated and imaged by USNO. The imaging was performed by using *Difmap* (see Section 2.2).

The set windows have been deleted and a new model was initialized with *startmod*. New windows were set with respect to the existing jet, as the jet has been neglected in the original analysis. As the data did not need to be calibrated again, the image only had to be cleaned and self-calibrated several times (different number of processes for each data set). When the total amount of flux is gained, a self-calibration on both amplitude and phase is performed. After this the procedure from *startmod* was repeated, but instead of using the self-calibration again, all windows were deleted and a final clean, the "deep clean", finished

<sup>3</sup><http://www.usno.navy.mil/USNO> (September 3, 2014)

<sup>4</sup><http://www.vlba.nrao.edu/> (September 3, 2014)

the imaging process.

This procedure was performed for every image in the S- and X-band and the final maps were plotted using ISIS (Interactive Spectral Interpretation System)<sup>5</sup>, a tool intended for the analysis of X-ray spectra by the MIT, but also a very effective plotting tool. The function to plot the VLBI map is included in the ISIS scripts, which are provided by the Dr. Karl Remeis observatory, Bamberg, Germany at <http://www.sternwarte.uni-erlangen.de/isis/>. An example of the final maps is shown in Figure 3.4, where the radio emission in the S- and X-band can be compared due to simultaneous observations. The beam is much larger at the lower frequency and it is also less sensitive compared to the X-band.

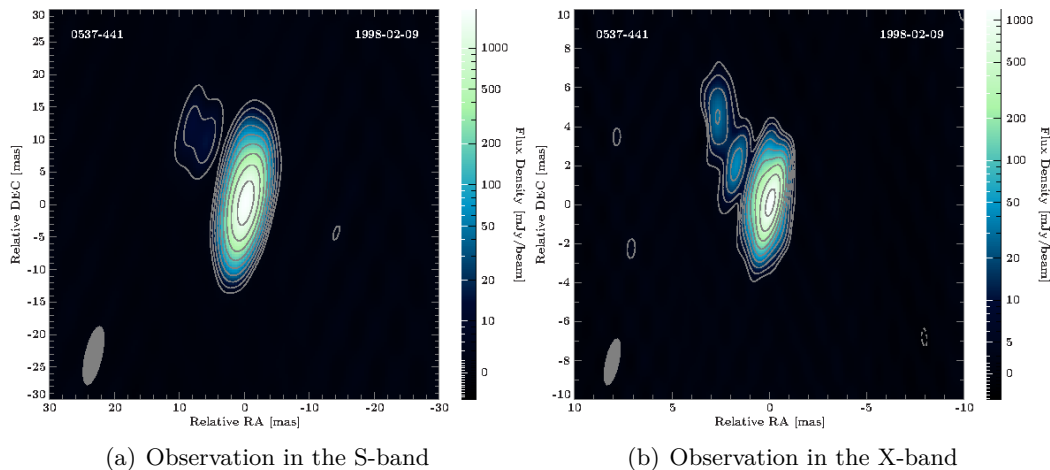


**Figure 3.4:** Images of the radio emission of PKS 0537–441 on September 2, 1998. In order to compare the emission region, it is important to notice the different scales of the source extension.

The total flux emitted from the source at each observation was written into a *FITS*-file using ISIS. The resulting light curve at both frequencies is shown in Figure 3.5. Mostly only small fluctuations can be seen, except for a significant increase of flux in mid 2010. Unfortunately, USNO doesn't provide observational data beyond this date, which makes it difficult to compare with the *Fermi* light curve. In Figure 3.6 an overplot of both bands is shown. One can see that the increase of the radio flux in 2010 coincides with the flare in the  $\gamma$ -ray band. In order to verify this behaviour, radio data after the last observation date from USNO is required.

Therefore radio data from other telescopes and arrays must be included in the study of a cross correlation. The additional instruments are introduced in the next section.

<sup>5</sup><http://space.mit.edu/cxc/isis/> (September 20, 2014)

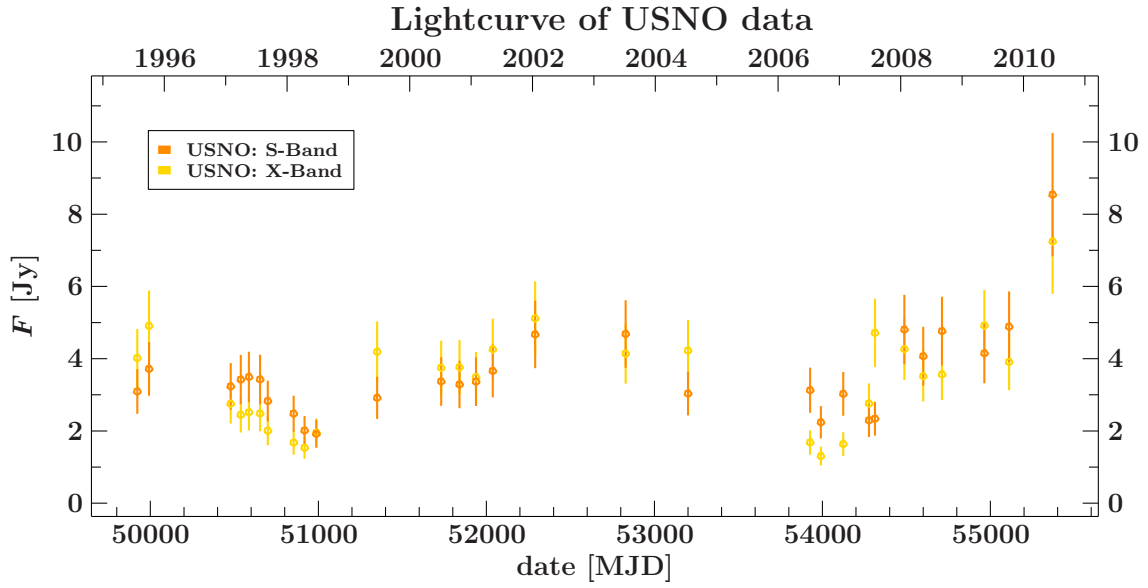


**Figure 3.5:** Light curve in the S- and X-band with data from VLBA.

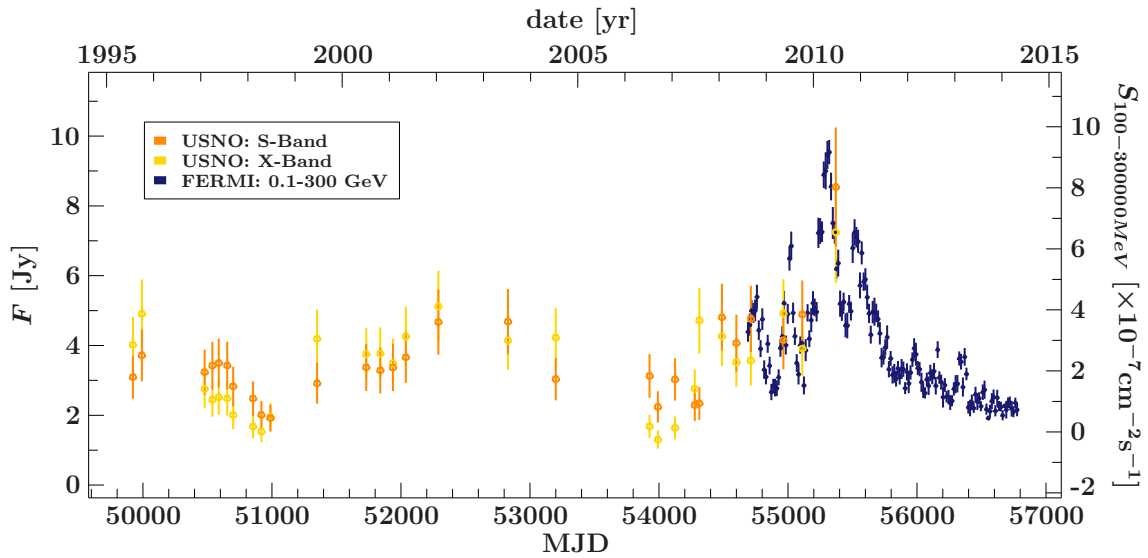


**Figure 3.6:** Comparison of the radio light curves from USNO (yellow and orange) and the  $\gamma$ -ray light curve from *Fermi* (blue). The left  $y$ -axis gives the radio flux of the USNO data, the right  $y$ -axis shows the flux of the  $\gamma$ -ray emission

## 3.3 Radio observations with ATCA, Ceduna and TANAMI

### 3.3.1 Brief introduction

#### ATCA

The Australia Telescope Compact Array (ATCA)<sup>6</sup> is part of the Australia Telescope National Facility (ATNF) and operates at the Paul Wild Observatory in Narrabri. The array contains six antennas with 22m dishes, gaining an angular resolution down to one arcsecond (1"). The single telescopes can be arranged in different constellations by aligning them from east to west on a trail with a maximum length of 6 km, or adding the north trail with a length of 214 m to create a more complex combination.

The array operates in several frequency bands, observations in four bands were included in this thesis. The selected frequencies are 4.8 GHz, 5.5 GHz, 8.6 GHz and 9.0 GHz, where 4.8 GHz and 8.6 GHz observations have been performed simultaneously, as well as 5.5 GHz and 9.0 GHz.

#### Ceduna

Ceduna<sup>7</sup> is a single dish telescope with 30 m diameter. It operates at a frequency of 6.7 GHz, in the X-band and the K-band. It reaches an angular resolution of about 11 arcseconds. Since 1995 the telescope is property of the University of Tasmania, but is part of the Australian VLBI array (LBA+) and TANAMI.



(a) Credit: <http://www.atnf.csiro.au/> (b) Credit: <http://en.wikipedia.org/wiki/resources/imagebank/telescopes.html> (September 4, 2014)  
ber 4, 2014)

**Figure 3.7:** On the left picture are five of the six ATCA telescopes aligned for observation. The radio telescope Ceduna is shown in the right picture.

<sup>6</sup><http://www.narrabri.atnf.csiro.au/> (September 4, 2014)

<sup>7</sup><http://www.phys.utas.edu.au/physics/Ceduna.html> (September 4, 2014)

### The TANAMI Multiwavelength program

The multiwavelength program TANAMI (Tracking Active Galactic Nuclei with Austral Milliarcsecond Interferometry)<sup>8</sup> was initialized in 2007 and its main purpose is to monitor relativistic jets of AGN in the Southern Hemisphere (Ohja et al., 2010). It acts as a counterbalance to radio observations on the Northern Sky. The observations are done at 8.4 GHz and 22.3 GHz with milliarcsecond resolution. Target sources are regularly observed at intervals of  $\sim 4$  months. Currently there are 13 telescopes or arrays taking part in this program.

One task of TANAMI is the study of the jet activity of blazars at radio wavelength together with the *Fermi* spacecraft. This hopefully will give answers to the questions whether  $\gamma$ -rays are produced in the core, jet or lobes and if  $\gamma$ -ray flares are accompanied by ejections of new jet components. The latter question is addressed in this thesis as a correlation is searched between  $\gamma$ - and radio emission (see Section 3.4).

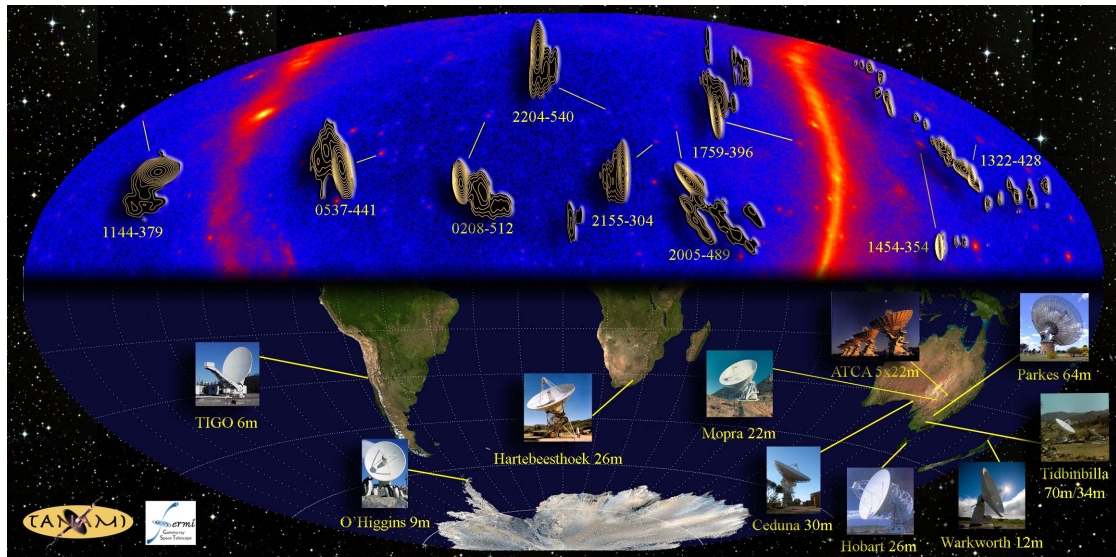


**Figure 3.8:** Illustration of all TANAMI telescopes and arrays below an image of the radio sky and its prominent AGN.

Credit: <http://pulsar.sternwarte.uni-erlangen.de/tanami/> (September 2, 2014)

### 3.3.2 Imaging of three TANAMI epochs

Since PKS 0537–441 is an interesting source due to its brightness in the  $\gamma$ -rays, it has been monitored by TANAMI on a regular basis in the X-band. The three latest observations are from May 8, 2010, August 13, 2011 and September 15, 2012. These had to be self-calibrated and imaged using *Difmap*. I applied the same procedure as in Section 2.2. As for the USNO data, the flux was computed via ISIS and the ISIS scripts. This package was also used to plot the maps, see Figure 3.9.

<sup>8</sup><http://pulsar.sternwarte.uni-erlangen.de/tanami/> (September 2, 2014)

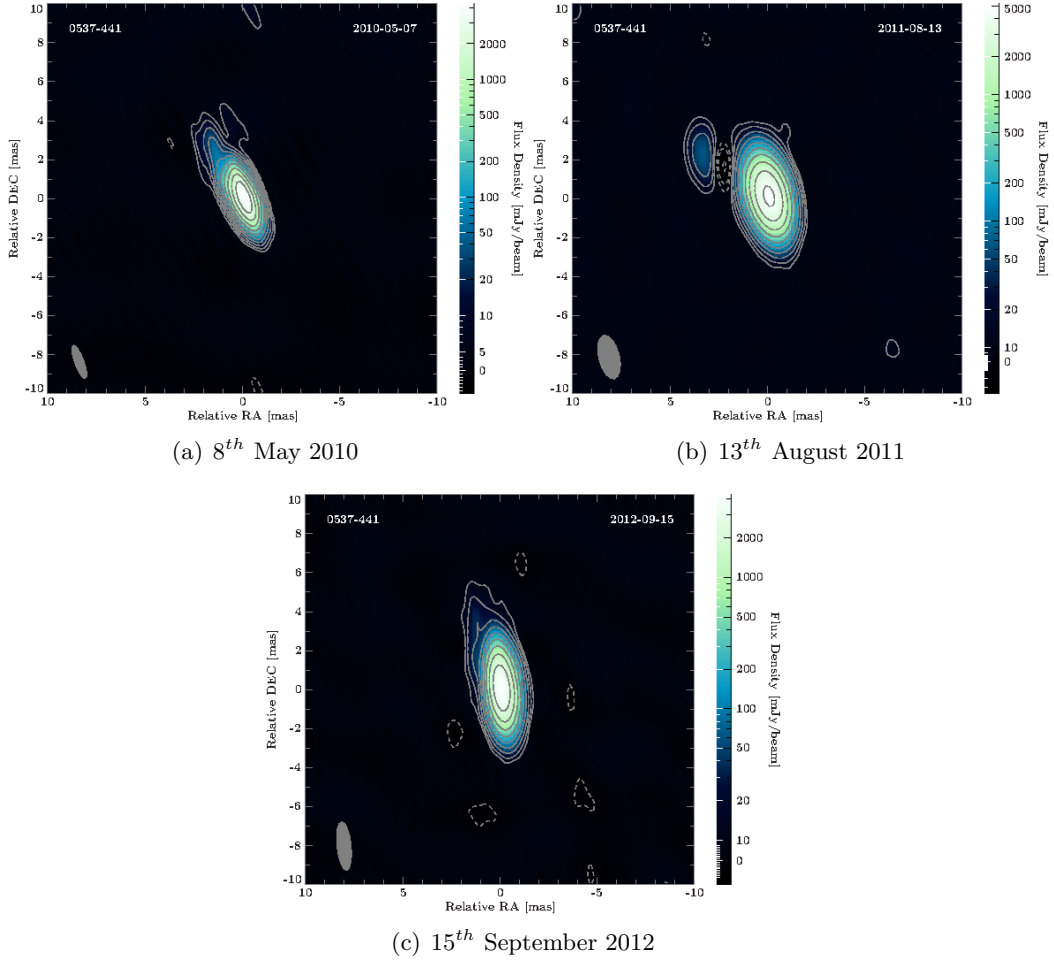


**Figure 3.9:** TANAMI images of the radio emission of PKS 0537–441 in the X-band. The observation dates are May 2010, August 2011 and September 2012

### 3.3.3 Light curve of all available radio data

In order to study the time evolution of the radio data, the USNO, ATCA, Ceduna and TANAMI data are plotted in one light curve, see Figure 3.10. The study of the spectral index  $\alpha$ , which gives the flatness of the spectrum, is included below the light curve. The relation between  $\alpha$  and the flux  $F$  is as follows:

$$F \sim \nu^\alpha \quad (3.1)$$

where  $\nu$  is the frequency of the emitted flux. Given simultaneous observations, the spectral index can be easily computed as

$$\alpha = \frac{\log(F_1) - \log(F_2)}{\log(\nu_1) - \log(\nu_2)} \quad (3.2)$$

If the spectral index is  $-0.5 < \alpha < 0.5$ , the spectrum is called a flat spectrum. All of the USNO observations in the S- and X-band as well as some ATCA observations were done

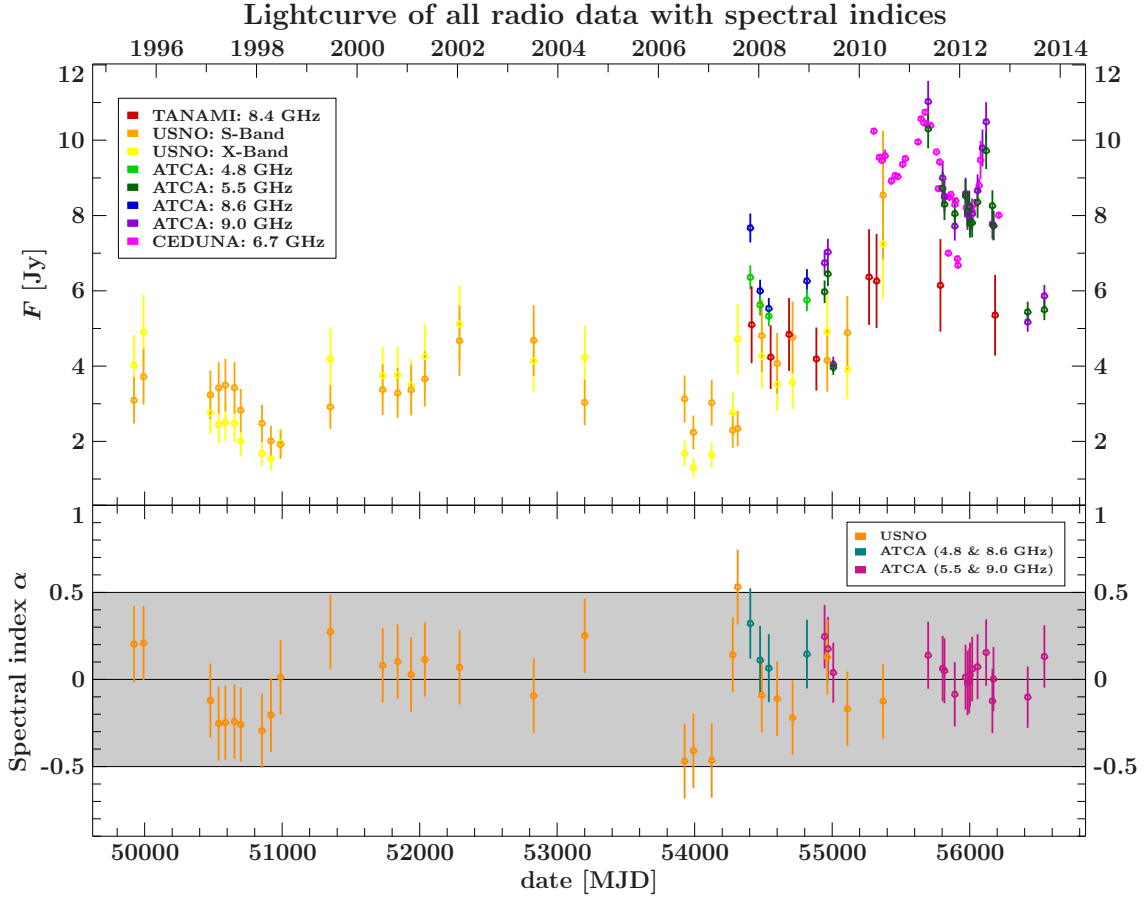


**Figure 3.10:** Light curve of all available radio data, partly analyzed in this thesis.

simultaneously respectively. This means that it is possible to have a look on the spectral index and check whether the spectrum is flat indeed. Figure 3.10 shows that all but four of the spectral indices are in the specified range, marked in gray, within their uncertainties. It is noticeable that now the light curve with additional data allows the comparison of different instruments. While TANAMI and USNO are approximately on the same flux level, ATCA is higher in flux at the same frequency. A quick analysis of the flux difference between ATCA and TANAMI is integrated to explain the reason for this circumstance.

### 3.3.3.1 Data comparison between ATCA and TANAMI

Four observations with TANAMI were performed almost contemporaneous to five ATCA observations, and because of the flat spectrum, data from TANAMI at 8.4 GHz and ATCA at 8.6 GHz and 9.0 GHz can be compared directly. The data points are shown in Figure 3.11. The analysis is carried out as a direct comparison of two flux values for each composition. The exact values can be found in Table 3.1.

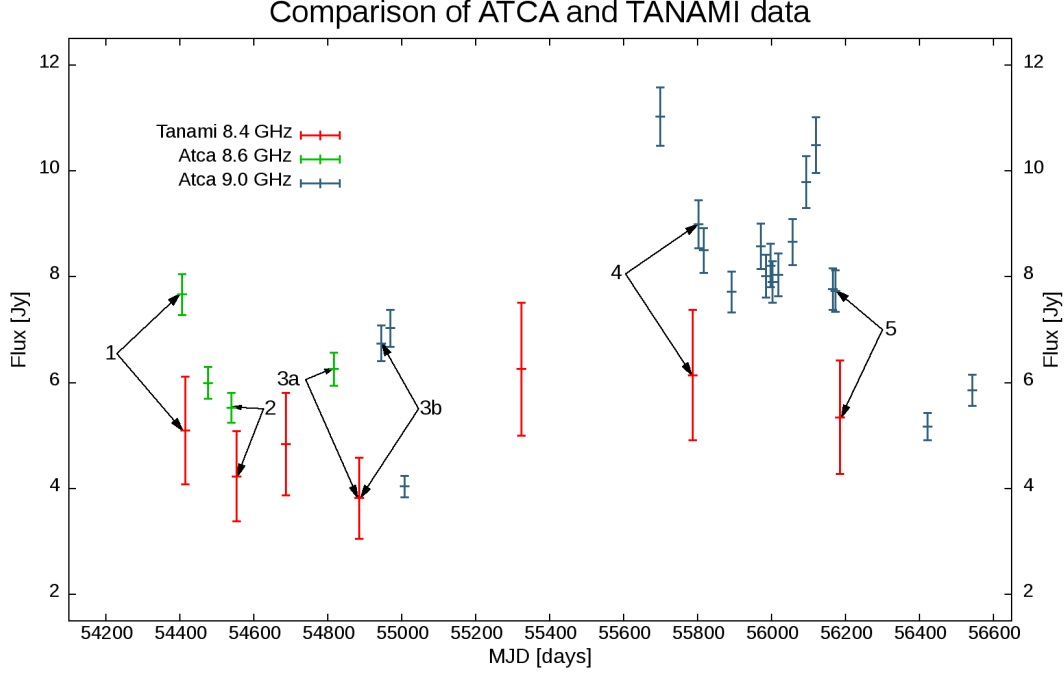


**Figure 3.11:** Data points of TANAMI and ATCA (at two frequencies). Compared fluxes are marked with arrows and a number for each affiliation.

	$f_A$	$MJD_A$	$MJD_T$	$Flux_A$ [Jy]	$Flux_T$ [Jy]	MJD	Flux [Jy]
1	8.6 GHz	54405	54414	$7.671 \pm 0.384$	$5.098 \pm 1.020$	9	$2.573 \pm 1.090$
2	8.6 GHz	54539	54553	$5.530 \pm 0.277$	$4.237 \pm 0.847$	14	$1.293 \pm 0.891$
3a	8.6 GHz	54816	54885	$6.263 \pm 0.313$	$3.824 \pm 0.765$	69	$2.439 \pm 0.827$
3b	9 GHz	54945	54885	$6.743 \pm 0.337$	$3.824 \pm 0.765$	60	$2.919 \pm 0.836$
4	9 GHz	55803	55787	$8.997 \pm 0.450$	$6.145 \pm 1.229$	16	$2.852 \pm 1.310$
5	9 GHz	56173	56185	$7.735 \pm 0.387$	$6.351 \pm 1.070$	12	$2.384 \pm 1.138$

**Table 3.1:** Results of the comparison of ATCA and TANAMI flux values.

The results are shown in Figure 3.12 together with the obtained mean flux difference between ATCA and TANAMI. On the  $y$ -axis the flux difference is shown, the  $x$ -axis is a measure for the time difference between both observations. The result for the mean flux difference is  $\overline{Flux_{A-T}} = 2.37 \pm 0.25 \text{ Jy}$ . The significant disagreement can be explained with the different angular resolution of the two arrays. While ATCA reaches a resolution of an arcsecond, TANAMI has a resolution of the order of milliarcseconds, which is an increase of  $10^3$  to ATCA. Therefore the TANAMI observations are more concentrated on inner jet, whereas ATCA gathers more radio emission, that surrounds the nucleus and might be part of an outer component of the jet. Under the assumption of non-variable radio emission for the larger jet scales on short timescales, we can conclude that the difference between both measurements gives a constant flux of the extended jet.

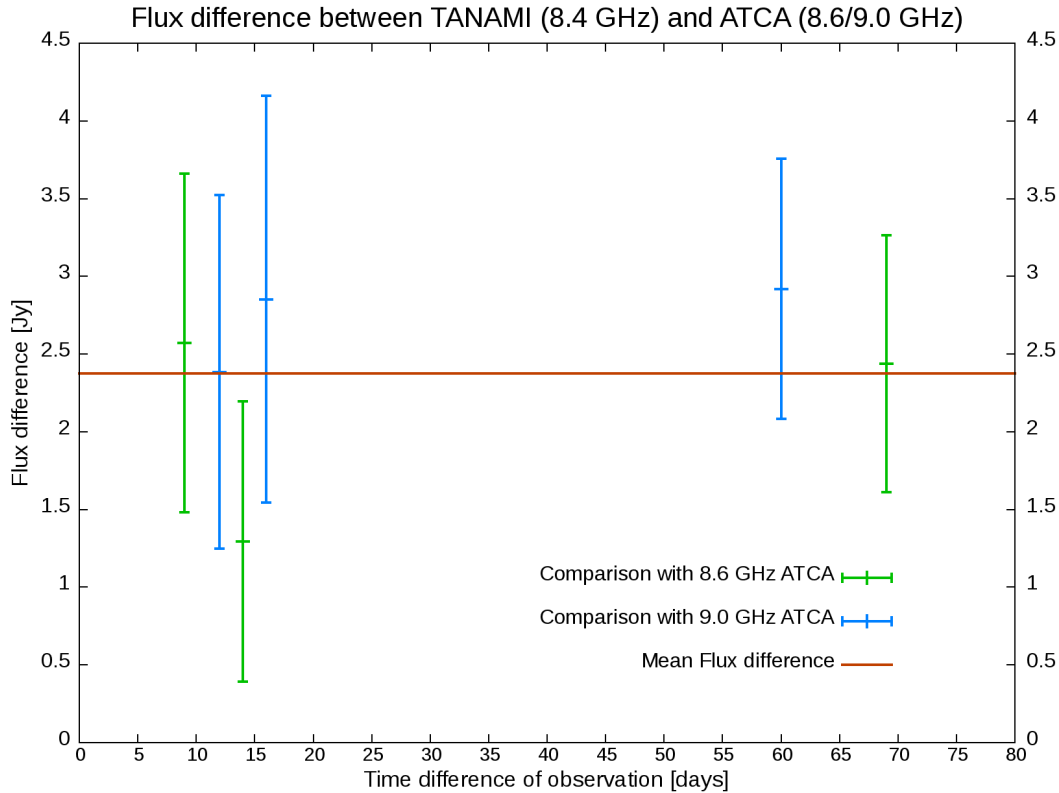


**Figure 3.12:** Resulting flux difference with computed mean flux.

### 3.4 Cross-correlation between the radio band and $\gamma$ -ray light curves

The additional observations of PKS 0537–441 now yield a light curve with a much greater overlap with the *Fermi* light curve. Now a cross-correlation analysis is performed to search for a possible correlation between  $\gamma$ -ray and radio emission of PKS 0537–441.

The goal is to search for a time lag between the two light curves, where a flare in one band leads to a flare in the other band. More generally one can compare dips and increasing/decreasing flux trend next to flares. Given the uneven sampling of the radio-band light curves, two methods for cross-correlation are considered: the Discrete Correlation Function (DCF; Edelson & Krolik 1988), and the Interpolated Correlation Function (ICF; White & Peterson 1994) in combination with the bootstrap method of Peterson et al. (1998) to derive the ICF lag error. In this thesis both methods are used to compare the results.

Because the available radio data are split up among different frequencies, only data with very similar photon energies can be combined into one light curve. The Ceduna data, with a frequency of 6.7 GHz, is treated separately; the 9.0 GHz ATCA light curve is also treated separately. Data from ATCA (8.6 GHz), USNO (8.6 GHz) and TANAMI (8.4 GHz) are combined into one light curve.

All three light curves are shown in Figure 3.13 - 3.15. The time intervals, however, are not similar in the plots, as well as the range of the flux on the  $y$ -axis.

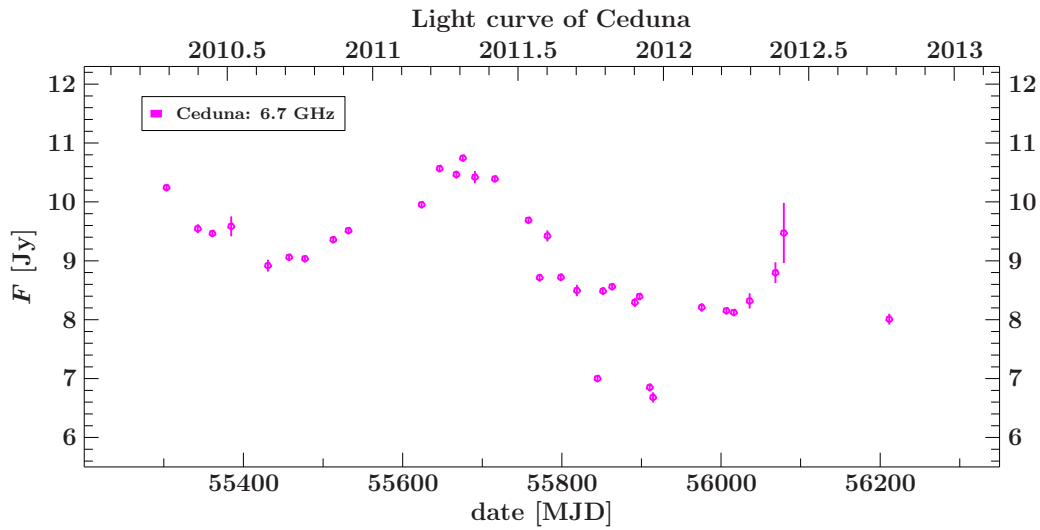


**Figure 3.13:** Light curve of Ceduna with 34 data points. A flare happens in the first half of 2011. The flux increases again in 2012.

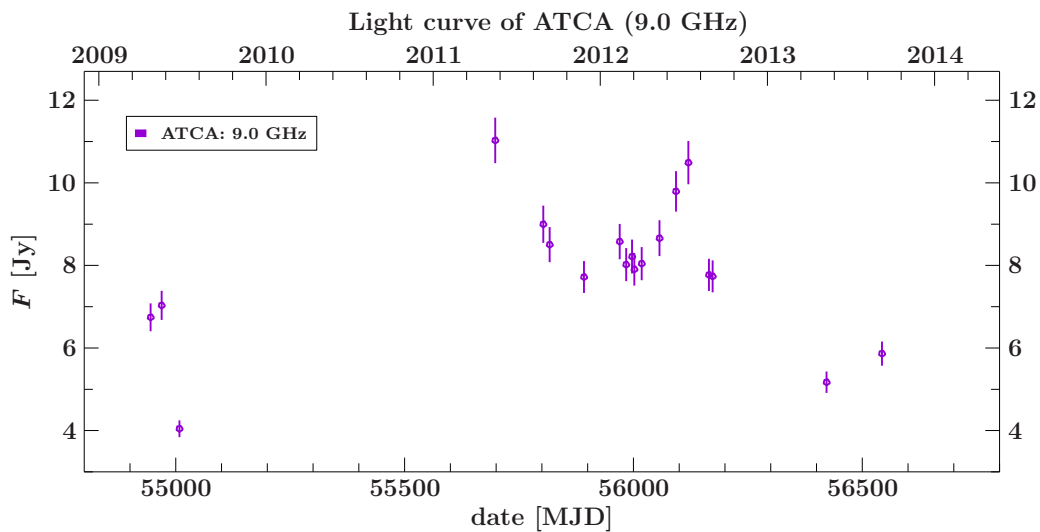


**Figure 3.14:** Light curve of ATCA at 9.0 GHz with 19 data points. A flare happens in mid 2012. The decrease of the flux in 2011 is a hint for another flare in the first half of 2011.

The main complication in this cross-correlation analysis is the sparseness of the radio light curves in comparison to the *Fermi* light curve. While the average sampling interval of *Fermi* is 14 days, the intervals for Ceduna, ATCA (9.0 GHz) and TANAMI/USNO/ATCA(8.6

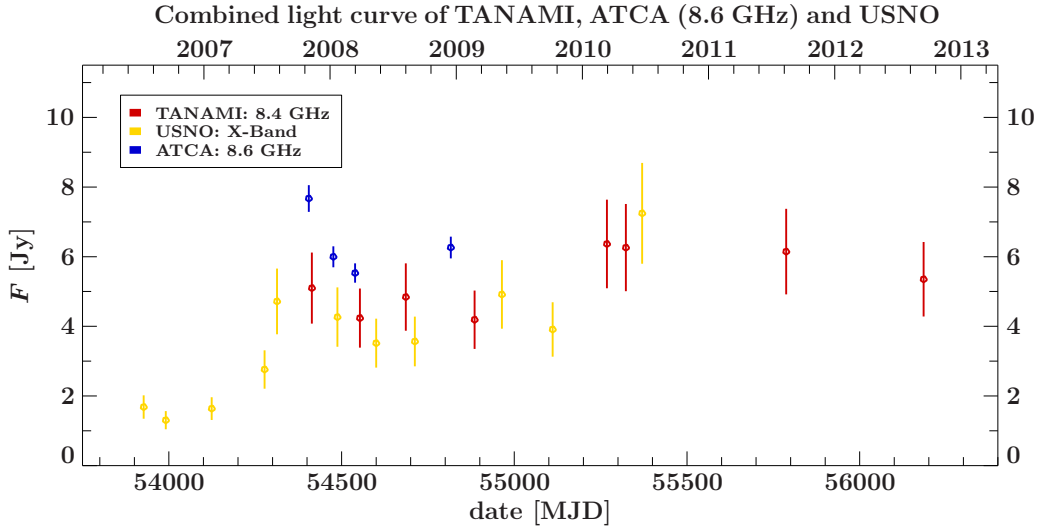


**Figure 3.15:** Combined light curve of TANAMI, USNO and ATCA (8.6 GHz) with 14 data points. A flare can be assumed in late 2007, but TANAMI and USNO show no clear trend. There is a hint on a flare in mid 2010 by the increase of the measured flux by USNO.

GHz) are 24, 162 and 89 days, respectively.

The light curves of ATCA (9.0 GHz) and TANAMI/USNO/ATCA(8.6 GHz) are less complete than the Ceduna light curve (see Figure 3.13, 3.14 and 3.15) and no distinctive trends can be seen, so we perform the cross-correlation with the Ceduna light curve only. We perform the ICF with a bin size of 7 days, which is half of the average bin size of *Fermi* observations, and assume that the intrinsic variability of the radio band is negligible on timescales less than 24 days. The ICF lag error is calculated using Flux Randomization (which takes the effects of flux errors on the ICF into account) and Random Subset Selection (which tests the effect gaps in the light curve). For the DCF, the bin size is 24 days. We used a wider bin size for the DCF than for the ICF in order to be conservative and to guarantee that enough data point pairs contribute to each DCF bin. This also reduces the point-to-point scatter of the DCF itself.

The resulting ICF and DCF are plotted together in Figure 3.16. In both functions, there is a broad peak with a positive lag, which means that the  $\gamma$ -ray light curve leads the radio light curve. For the ICF, a peak correlation coefficient of  $r_{\text{corr ICF}} = 0.592$  is found at a peak lag of  $98 \pm 72$  days. With the DCF, the peak is  $r_{\text{corr DCF}} = 0.6270 \pm 0.1067$  at a peak lag of 96 days. As a check on this derived time lag, we overplot both light curves as shown in Figure 3.17; the time lag is realized by moving the radio light curve backwards by 97 days (the mean of the ICF and DCF peak time lags). Additionally, the light curves were divided by their respective mean values for a more direct comparison. One can see in the overplot that the peaks near MJD  $\sim 55500$ , the subsequent flux decreases, and the increasing trends at MJD  $\sim 55600 - \sim 56000$  match up well and seem to be driving the correlation. However there seems to be no matching radio component for the biggest  $\gamma$ -ray flare. Additionally the minimum/maximum GeV fluxes span a wider relative range

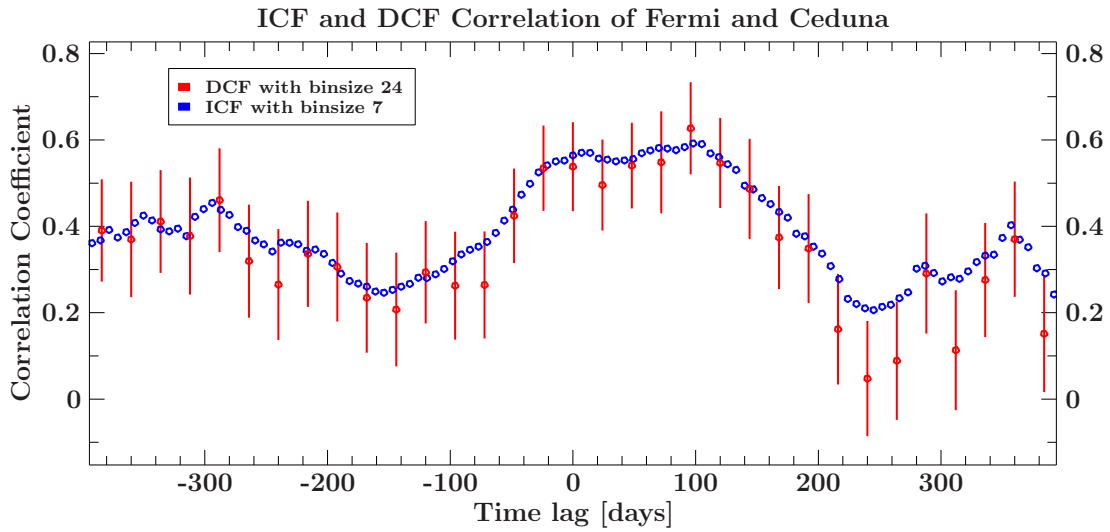


**Figure 3.16:** Resulting cross-correlation functions using the ICF and DCF; a positive lag denotes  $\gamma$ -ray leads radio

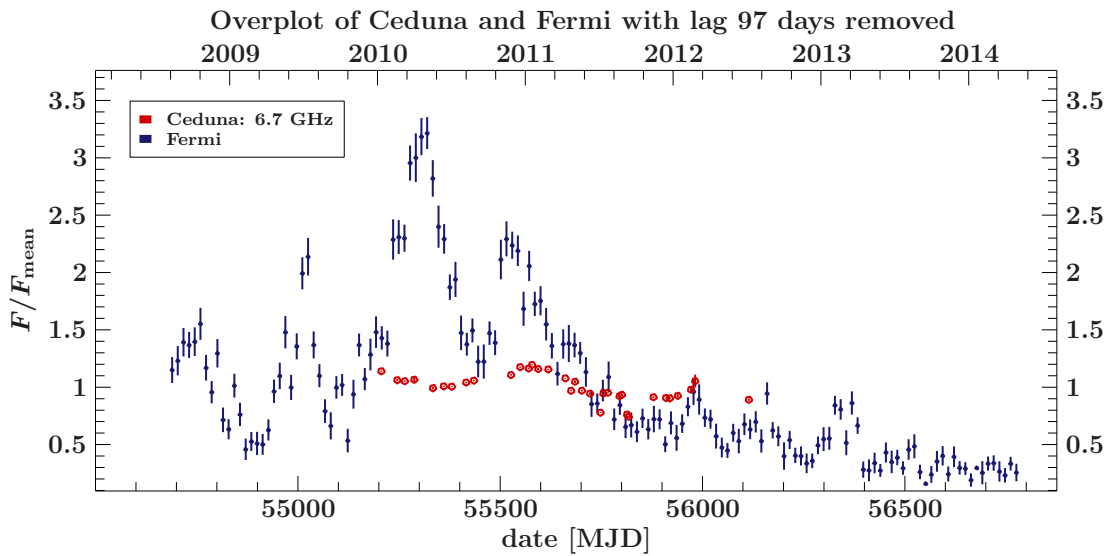


**Figure 3.17:** Overplot of *Fermi* and Ceduna light curve with a time lag of 97 days.

(with factors of  $\sim 2 - 3$  above/below mean) compared to the radio band data ( $\sim 20 - 30\%$  above/below mean). These factors may be the reason for the relatively low peak correlation coefficients. Changing the bin size (by factors of 2 and 0.5) yields results consistent with the present analysis.



## 4 Discussion and outlook

The active galaxy PKS 0537–441 shows flux variability (flares, increasing and decreasing trends) in the  $\gamma$ -rays, where the brightest flare happened in the first half of 2010 and shows a maximum flux of more than 3 times the mean flux. From the radio data of USNO, one can also find an upward trend of the flux in the S- and X-band, which starts in 2008. The analysis of a possible correlation of  $\gamma$ -ray and radio emission was impractical to do because the *Fermi* mission only started in 2008, whereas USNO gathered data only from 1995 until 2010.

In order to create a much better overlap between the  $\gamma$ -ray data set and the observations of USNO, the originally considered data set of USNO radio data had to be combined with radio observations from other telescopes and arrays. The data sets from Ceduna, ATCA and TANAMI extended the view on the behaviour of the radio emission (in the S- and X-band) of the blazar after 2010. Since on some dates observations from TANAMI and ATCA were performed nearly simultaneously at nearly the same frequency, it is noticeable that the values for the fluxes seem to differ at a certain offset. This occurs because the arrays have different angular resolutions that lead to these features.

Although the observations of the three added radio instruments were more regular than the observations by USNO, they have not been performed as continuous as the observations by *Fermi*, which operates in an all-sky-survey mode. Not all of the radio data can be combined into one light curve, so the radio light curves available for cross-correlation are still sparse. The only suitable data set is therefore from Ceduna, because the *Fermi* light curve covers the time range of its observations completely and it has the most data points compared to the other radio data sets.

With *Fermi* and Ceduna only, the cross-correlation which is performed in this thesis by using the ICF and the DCF, is possible and gives a time lag of  $\sim 97$  days with a correlation coefficient of about 60% with both methods. This value is quite low for a correlation, but it is not possible to improve the result by changing the bin size. Regarding the sparse sampling of the radio light curves, the outcome of the cross-correlation analysis is sufficient. The positive time lag is in agreement with the assumption that flares first appear in the  $\gamma$ -rays. Then they move energetically downwards along the whole electromagnetic spectrum, when the emission of the AGN spreads in space.

Compared to the previous study by D'Ammando et al. (2013), where the time lag between the  $\gamma$ -ray and the R-band radio light curve is  $\sim 3$  days, the determined time lag in thesis is quite large. To prove the result of this thesis trustworthy, it is necessary to repeat the cross-correlation analysis with data samplings with smaller time lags between the observations.



# Bibliography

- Atwood W.B. et al., 2009, ApJ, 679, 1071
- Burke B.F., Graham-Smith F., 2010, An Introduction to Radio Astronomy, Cambridge, Cambridge University Press
- Beckmann V., Shrader C., 2012, Active Galactic Nuclei, Weinheim, WILEY-VCH Verlag
- Bennett A.S., 1962, MNRAS, 68, 163
- Boettcher M., Harris D.E., Krawczynski H., 2012, Relativistic Jets from Active Galactic Nuclei, Weinheim, WILEY-VCH Verlag
- Bridle A.H. et al., 1994, AJ, 108, 766
- Ciaramella A. et al., 2004, A&A, 419, 485
- Curtis H.D., 1918, PLicO, 13, 9
- D'Ammando F. et al., 2013, MNRAS, 431, 2481
- Di Matteo T., Springel V., Hernquist L., 2005, Nature, 433, 604
- Edelson R., Krolik J., 1988, ApJ, 333, 646
- Fanaroff B.L., Riley J.M., 1974, MNRAS, 167, 31P
- Ghisellini G. et al., 2011, MNRAS, 414, 2674
- Giommi P., Ansari S.G., Micol A., 1995, A&AS, 109, 267
- Harris G.L.H., Rejkuba M., Harris E.W., 2009, PASA in press
- Heidt J., Wagner S.J., 1996, A&A, 305, 42
- Hoffmeister C., 1929, Astronomische Nachrichten, 236, 233
- Hogg D.E., MacDonald G.H., Conway R.G., Wade C.M., 1969, AJ, 74, 1206
- Hoyle F., Fowler W.A., 1963, MNRAS, 125, 169
- Kappes A., 2013, Bachelor thesis
- Kellermann K.I. et al., 1989, AJ, 98, 1195

- Khachikian E.Y., Weedman D.W., 1974, *ApJ*, 192, 518
- Laing R.A., Bridle A.H., 1987, *MNRAS*, 228, 557
- Liller Wm., 1974, *ApJ*, 189, L101
- Maraschi et al., 1985, *ApJ*, 294, 615
- Müller C., 2010, Diploma thesis
- Ohja R. et al., 2010, *A&A*, 519, A45
- Peterson B.A. et al., 1976, *ApJ*, 207, L5
- Peterson B.A. et al., 1998, *PASP*, 110, 660
- Romero G.E., Surpi G., Vucetich H., 1995, *A&A*, 301, 641
- Romero G.E. et al., 2002, *A&A*, 390, 431
- Salpeter E.E., 1964, *ApJ*, 140, 796
- Schmidt M., 1963, *Nature*, 197, 1040
- Seyfert C.K., 1943, *ApJ*, 97, 28
- Shakura N.I., Sunyaev R.A., 1973, *A&A*, 24, 337
- Tanzi E.G. et al., 1986, *ApJ*, 311, L13
- Taylor G., 1997, *The Difmap Cookbook*
- Treves A. et al., 1993, *ApJ*, 406, 447
- Urry C.M., Padovani P., 1995, *PASP*, 107, 803
- Wagner S.J., Witzel A., 1995, *ARA&A*, 33, 163
- White R., Peterson B. M., 1994, *PASP*, 106, 879
- Woltjer L., 1959, *ApJ*, 130, 38

# Acknowledgements

This thesis would not exist without the help, support and knowledge of many people. First I want to express my gratitude to my supervisor Jörn Wilms, for his help, support and enabling me to write my thesis in the field of astrophysics. I would like to thank Felicia Krauß for her help concerning the Fermi data analysis, her patience with a beginner's mistakes and her advices for my thesis. I appreciate Cornelia Müller for helping me with VLBI mapping and for her constructive suggestions improving my thesis. I want to thank Alex Markowitz, who explained cross-correlation of observational data to me and helped me with the analysis. I'm thankful that my supervisor Matthias Kadler from the university of Würzburg and his group helped me with the radio data. The people of the Remeis Observatory created a welcoming, pleasant and inspiring environment - I enjoyed it very much working there on my thesis. Last but not least I want to express my thanks to my family and friends for their support.



# Erklärung

Hiermit erkläre ich, dass ich die vorliegende Arbeit selbstständig und nur unter Verwendung der angegebenen Hilfsmittel angefertigt habe und erstmalig einreiche.

---

Ort, Datum

---

Andrea Gokus